Research Square

Preprints are preliminary reports that have not undergone peer review.
They should not be considered conclusive, used to inform clinical practice,
or referenced by the media as validated information.

Magnetoplasmonic keychains for multiplexed polarization-encoded tags

Tae Soup Shim

tsshim@ajou.ac.kr

Ajou University https://orcid.org/0000-0003-2414-1599

Jin Hyeok Park

Ajou University https://orcid.org/0009-0007-3967-3623

Hyojung Kang

Ewha Womans University https://orcid.org/0000-0003-2015-4552

Seojin Lee

Ewha Womans University

Ye-Eun Choi

Ewha Womans University

Hyerim Hwang

Ewha Womans University https://orcid.org/0000-0001-8098-6030

So-Jung Park

Ewha Womans University https://orcid.org/0000-0002-6364-3754

Article

Keywords:

Posted Date: October 28th, 2026

DOI: https://doi.org/10.21203/rs.3.rs-10816876/v1

License: This work is licensed under a Creative Commons Attribution 4.0 International License.
Read Full License

Additional Declarations: There is **NO** Competing Interest.

Magnetoplasmonic keychains for multiplexed polarization-encoded tags

Jin Hyeok Park,[1, †] Hyojung Kang,[2, †] Seojin Lee,[3,4] Ye-Eun Choi, [3,4] Hyerim Hwang,[3,4] So-Jung Park[2,3,5,] and Tae Soup Shim[1,6,*]*

[1]Department of Energy Systems Research, Ajou University, Suwon 16499, Republic of Korea

[2]Department of Chemistry and Nanoscience, Ewha Womans University, Seoul 03760, Republic of Korea

[3]Institute for Multiscale Matter and Systems (IMMS), Ewha Womans University, Seoul 03760, Republic of Korea

[4]Department of Chemical Engineering and Materials Science, Ewha Womans University, Seoul 03760, Republic of Korea

[5]Graduate Program in Innovative Biomaterials Convergence, Ewha Womans University, Seoul 03760, Republic of Korea

[6]Department of Chemical Engineering, Ajou University, Suwon 16499, Republic of Korea

†These authors contributed equally to this work.

*Corresponding authors. Email: sojungpark@ewha.ac.kr, tsshim@ajou.ac.kr

Abstract: Physical security tags are becoming increasingly vulnerable to replication as computational capabilities continue to advance. Here, we present a magnetoplasmonic platform that converts complex three-dimensional magnetic field configurations into polarization-resolved optical signatures through magnetically programmable alignment of plasmonic nanostructures. Unlike physical unclonable functions, which rely on intrinsic randomness, our platform enables deterministic information encoding and key-dependent decoding through a magnetoplasmonic keychain (K_{MP}). Spatial multiplexing of three independent magnetic configurations within a 60-pixel architecture generates an encoding space on the order of 10^{44}. Without access to K_{MP}, decoding is infeasible because the inverse problem is fundamentally ill-posed, preventing recovery of the encoded information even with machine-learning models. In contrast, when K_{MP} is available, encoded information can be rapidly and accurately reconstructed through simple optical readout. These results establish a physically enforced encryption framework, complementing computational cryptography and providing a scalable platform for secure authentication and information storage.

Physical security tags designed for authentication are becoming increasingly vulnerable to replication as advances in computation enable rapid analysis and reconstruction of exposed physical patterns[1–3]. An adversary with access to an exposed physical pattern can, in principle, extract or reproduce encoded information in many existing physical authentication systems, which encode information in directly readable structural, optical, or electronic signatures[4,5]. In contrast, modern digital cryptography ensures security through a secret-key paradigm, in which encryption is straightforward, whereas decryption without knowledge of the secret key is computationally infeasible owing to the large size of the key space[6]. Translating this paradigm to physical security requires a physical analogue of Kerckhoffs' principle, in which security depends on possession of a physical key rather than concealment of the encoding mechanism[7]. As machine-learning-based attacks capable of exploiting subtle correlations in physical signals continue to advance, the absence of such key-based protection has emerged as a critical limitation of existing physical authentication technologies, including physical unclonable functions (PUFs), which provide intrinsic uniqueness but lack a scalable framework for secret-key management[8,9].

Optical encryption conceals information through light–matter interactions and enables its recovery under specific optical readout conditions, such as the polarization state[10–12], wavelength[13,14], orbital angular momentum modes[15,16], and combinations thereof[17–19]. Among these approaches, plasmonic optical encryption has attracted considerable interest because localized surface plasmon resonance (SPR) is exquisitely sensitive to nanoscale geometry, enabling diverse optical encoding through tunable color responses[20–23]. However, existing plasmonic encryption systems are typically fabricated using deterministic nanofabrication techniques, such as focused ion beam milling[24,25], electron beam lithography[26,27], or direct laser writing[28–30]. Although these approaches enable arbitrary nanoscale patterning with high spatial resolution, they are typically costly, offer limited throughput, and produce structurally fixed, fully observable patterns. Polarization-engineered plasmonic architectures have further

expanded the complexity of optical responses[31–35]. However, they inherently lack hidden physical degrees of freedom that can serve as secure physical keys. Consequently, information recovery generally requires additional optical readout and computational decoding procedures, limiting practical deployment outside laboratory environments. An ideal physical authentication platform should instead embed high-dimensional hidden physical complexity during fabrication while enabling authentication through simple image-based optical readout.

In this study, we introduce a magnetically encoded plasmonic encryption platform based on magnetically controllable plasmonic nanoparticles (MPs) whose orientation and plasmonic modes can be remotely and dynamically programmed by external magnetic fields[36]. By dispersing MPs in a photopolymerizable precursor, magnetic field distributions can be directly written into matter as polarization-dependent optical states[37–39]**.** Spatially varying magnetic fields align nanorods along local field directions, transforming the input of three-dimensional magnetic field configurations into rich plasmonic color patterns, readable via polarization-resolved imaging. Subsequent polymerization permanently fixes these orientation states, establishing a one-to-one mapping between magnetic field configurations and optically decodable plasmonic patterns. To enable secure decoding, we introduce a magnetoplasmonic keychain (K_{MP}), which specifies how magnetic configurations are spatially assigned within a multiplexed plasmonic tag. In this system, information can be readily encoded and decoded when K_{MP} is available, whereas decoding without K_{MP} is fundamentally infeasible. This cross-domain strategy establishes a physically enforced encryption platform that combines deterministic encoding with key-dependent decoding, representing a shift from conventional pattern-based security to physically encoded key-based security.

Results and Discussion

Expanded plasmonic color space through programmable magnetic alignment and polarization-controlled optical responses

The MPs consisted of an elongated gold nanorod core supporting longitudinal (LSPR) and transverse (TSPR) surface plasmon modes, a superparamagnetic iron oxide interlayer for rapid magnetic alignment, and an outer silica shell for colloidal stability (**Fig. 1a** and **Supplementary Fig. 1**). The final MPs exhibited characteristic TSPR and LSPR bands at 521 and 800 nm, respectively. Comparisons between single- and dual-polarizer configurations (**Fig. 1b**) reveal distinct mechanisms of color generation. Under a single polarizer, the observed color was governed primarily by selective excitation of the LSPR or TSPR modes according to the relative orientation between the MP and polarization axis (Fig. 1b, i and **Supplementary Fig. 2**). By contrast, in the dual-polarizer configuration (Fig. 1b, ii) with the input polarizer set at 45° or 135°, plasmon-mediated birefringence introduces a phase retardation between polarization components parallel and perpendicular to the MP orientation, allowing the transmitted color to be continuously tuned by varying the output polarizer angle. These characteristics are reflected in the MP orientation-dependent color libraries shown in **Fig. 1c**. Under the single-polarizer configuration, the MP array exhibited only modest color variations as the MP orientation was rotated from 0° to 180° (Fig. 1c, top). In contrast, the dual-polarizer configuration with input and output polarizer angles of 135° and 60°, respectively, generated substantially broader color gamut, including numerous hues inaccessible under the single-polarizer configuration (Fig. 1c, bottom). Transmission spectra represented as heatmaps (**Fig. 1d**) confirmed that the single-polarizer configuration exhibited discrete switching between the LSPR and TSPR modes, whereas the dual-polarizer configuration produced continuous spectral evolution as the output polarizer angle varied. Correspondingly, Commission Internationale de l'éclairage (CIE) 1931 chromaticity diagram (**Fig. 1e**) shows that the dual-polarizer set-up spans a substantially broader area than the single-polarizer case. These results demonstrate that combining magnetic

alignment with polarization-resolved optical readout expands the accessible optical response space of plasmonic materials, thereby establishing the optical basis for high-capacity information encoding.

The rapid magnetic alignment of MPs enables immediate and permanent fixation of plasmonic colors by photopolymerization. **Fig. 1f** schematically illustrates the sequence of magnetic alignment and subsequent fixation. To achieve this, we developed a photopolymerizable plasmonic ink (PPI), consisting of MPs dispersed in a poly(ethylene glycol) diacrylate (PEGDA) solution containing a photoinitiator (see Supporting Information for experimental details). Application of a magnetic field produced distinct polarization-dependent colors through collective MP alignment, while photopolymerization immobilized the aligned structures, preserving their optical response after removal of the field. Time-resolved optical measurements under a rotating magnetic field revealed rapid and reversible modulation of the optical signal in both water and the more viscous PPI, indicating that the MPs continuously realigned with changes in the field direction (**Fig. 1g**). Fast Fourier transform (FFT) analysis showed a sharp peak at twice the rotation frequency (**Fig. 1h**), consistent with two optical cycles per full rotation of the magnetic field. After polymerization, no periodic optical modulation was observed under a rotating magnetic field, confirming that submicrometer-sized MPs were permanently immobilized within the cross-linked PPI network, preserving their magnetically programmed orientations.

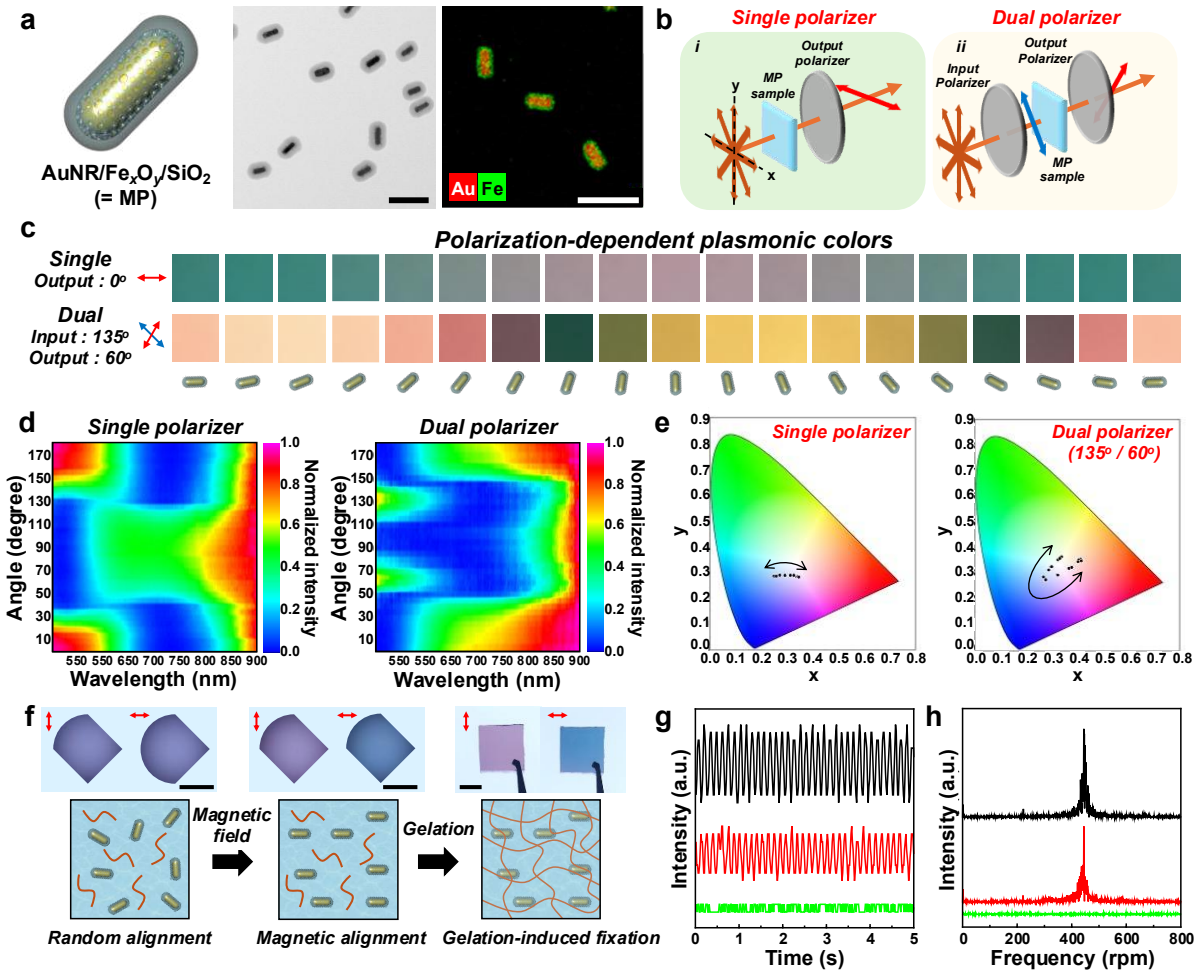


Fig. 1 | Polarization-dependent plasmonic colors of magnetically oriented MPs. a Schematic illustration, TEM image, and elemental mapping of MPs composed of gold nanorod (AuNR) core, iron oxide interlayer (Fe_xO_y) and silica shell (SiO_2). Red and green colors in EDS map indicate Au and Fe, respectively. **b** Schematic diagrams of the optical setups for the single (i) and dual (ii) polarizers. **c** Color library of polarization-dependent plasmonic responses for linearly aligned MPs with varying MP orientations (0~180°) under single (top) and dual (bottom) polarizer conditions. The input and output polarization directions are indicated by blue and red arrows, respectively. The polarizer angle is defined as the counterclockwise angle measured from the x-axis. **d** Angle-resolved transmittance spectra plotted as a two-dimensional color map under single and dual polarizer configurations. **e** CIE 1931 color space mapping of plasmonic colors according to the MP angles under single and dual polarizers. **f** Schematic illustration (bottom) and photographs (top) taken under single polarizer configuration demonstrating the magnetic alignment and fixation of MPs within a hydrogel matrix. The magnetic field was applied along the x axis. The red arrows in the photographs indicate the output polarizer angle. **g** Time-resolved extinction modulation of MPs under a rotating magnetic field at 200 rpm in water (black), 50% PEGDA

solution (red) and cross-linked PEGDA hydrogel (green). **h** FFT conversion of the magnetic modulation data in (g). Scale bar: (a) 200 nm and (f) 5 mm.

Spatial programming of polarization-encoded plasmonic architectures

Magnetic field-directed color states were integrated with micropatterning to spatially program MP orientations, generating polarization-dependent optical patterns that function as information-bearing microstructures. **Fig. 2a** illustrates the sequential photopolymerization of the PPI while varying the magnetic field direction, producing multi-domain structures with distinct polarization responses. The sun- and cloud-shaped patterns (**Fig. 2b**) containing MPs aligned at 90° and 0°, respectively, appeared in identical colors when the input and output polarizers were aligned at the same angle (Fig. 2b, i). Under a 45°/135° cross-polarizer condition, the orthogonally aligned MP domains also exhibited identical colors because they produced equivalent birefringent phase retardation (Fig. 2b, ii). Rotating the output polarizer angle broke this optical symmetry, producing distinct color transitions in the two regions according to their MP orientations (Fig. 2b, iii-iv). The same principle was applied to polarization-dependent retrieval of hidden number information in micropatterned dot arrays (Fig. 2b, v-viii). **Fig. 2c** demonstrates that polarization-dependent plasmonic color patterns can be fabricated with feature sizes of several tens of micrometers, highlighting the potential of the magnetoplasmonic platform for high-resolution plasmonic patterning.

For digitally addressable encoding, PPI was introduced into poly(dimethylsiloxane) (PDMS) microwell arrays at predefined spatial coordinates using an automated dispenser, followed by magnetic alignment and fixation to encode symbols ‘O’ and ‘X’ (**Fig. 2d**). Pixel-wise color analyses under appropriate polarization conditions converted the resulting plasmonic responses into high-contrast digital patterns, enabling recovery of the encoded symbols (**Fig. 2e**). A pixelated optical pattern consisting of a 25 × 13 array with a unit pixel size of approximately 2 mm was further prepared (**Fig. 2f**). While the encoded information became increasingly

difficult to distinguish at this pixel size, computational color analysis successfully reconstructed the encoded message of "NANO GOLD". These results demonstrate that integrating photopatterned hydrogels with magnetically programmed MP alignment provides a versatile platform for visually concealed yet optically decodable encryption.

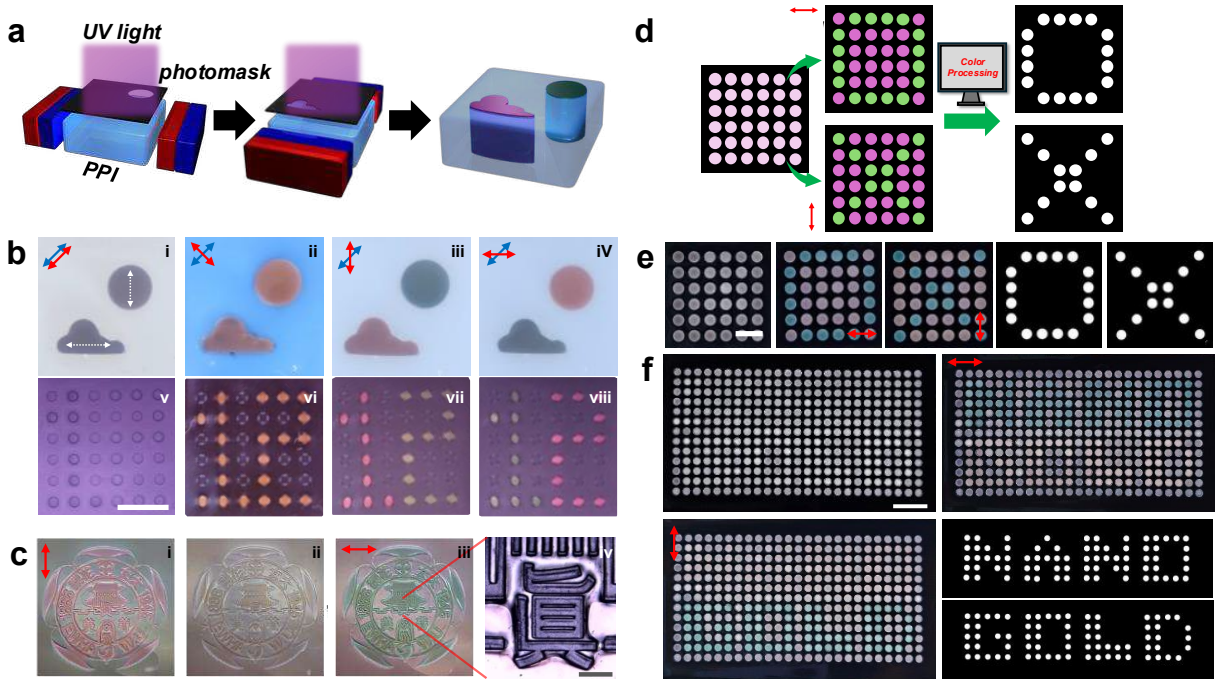


Fig. 2 | Spatially programmed plasmonic patterns obtained via magnetic alignment. a Schematic of the stepwise magnetic alignment and photopatterning process used to generate the spatially programmed MP orientations shown in panels (b) and (c). **b** Photographs of plasmonic hydrogel patterns with spatially programmed MP alignment under a dual-polarizer configuration. Blue and red arrows indicate input and output polarizer angles, respectively. (i-iv) A sun-cloud pattern, incorporating MPs oriented at 0° and 90°, respectively (marked with dotted white arrows in i), imaged with the output polarizer set to 45° (i), 135° (ii), 90° (iii), and 180° (iv). (v-viii) Micropatterned dot arrays incorporating MPs with distinct orientations, revealing hidden numbers under a dual polarizer configuration. MPs in digits 1 and 2 are aligned at 90° and 0°, respectively, while those in the remaining dots and background are randomly oriented. **c** Photographs (i-iii) and an optical microscope image (iv) of a micropatterned plasmonic hydrogel. Images i, iii, and iv were obtained under the single-polarizer configuration (output polarizer direction indicated by the red arrow), whereas image ii was acquired without a polarizer. **d** Schematic illustration of pixelated patterns encoding by dispensing the PPI into PDMS microwell arrays, followed by image-based processing, as used in panels (e) and (f). **e-f** Photographs under unpolarized

and single polarizer conditions and corresponding high-contrast images obtained by extracting specific color channels from pixelated arrays, showing spatially encoded text, (e) “O” and “X”, and (f) "NANO GOLD". Scale bar: (b) 5 mm, (c) 500 μm, (e) 10 mm.

Deterministic mapping of complex 3D magnetic fields into plasmonic patterns

Complex magnetic fields enable deterministic three-dimensional programming of MP orientations within the polymerized PPI, providing a route to encode intricate magnetic field topologies into information-rich plasmonic patterns. To generate such fields, we fabricated a circular holder accommodating eight permanent cubic magnets at fixed angular intervals around the sample (**Fig. 3a**). Six orientation states were defined for each magnet: inward (*I*), outward (*O*), left (*L*), right (*R*), normal (*N*), and blank (*B*). Magnetic configurations were denoted by eight-character sequences (e.g., *IIORORIL*), in which each character represents the orientation of a single magnet. The system yields 1.48×10^6 physically distinct MP orientation patterns (**Supplementary Note 1**), excluding complementary in-plane pairs that produce equivalent patterns (**Supplementary Fig. 3**). **Fig. 3b** depicts representative symmetric and asymmetric arrangements of cubic magnets (e.g., *ORILORIL* and *IIORORIL*), each generating a distinct spatially complex magnetic field distribution. Importantly, these fields, in turn, dictate the three-dimensional orientation of the MPs, defined by their in-plane orientation and out-of-plane tilt angle (θ_z) (**Fig. 3c**). As θ_z increased, the analyzer-angle dependence of the plasmonic color progressively diminished, reflecting the increasingly isotropic in-plane projection of the MP orientation (**Fig. 3d** and **Supplementary Fig. 4**). This behavior was quantified by a linear decrease in the polarization-dependent color difference (ΔE) with increasing θ_z (**Fig. 3e**). An experimental color library mapping polarizer configurations and MP orientations to plasmonic colors was constructed (**Supplementary Note 2** and **Supplementary Fig. 5**). Local MP orientations extracted from calculated three-dimensional magnetic field distributions were then mapped to plasmonic colors using this experimentally calibrated library (**Supplementary Note 3**), enabling deterministic translation of magnetic field geometry into polarization-resolved plasmonic color patterns. This strategy was applied to convert approximately 120,000 distinct complex magnetic field configurations into corresponding plasmonic color patterns. The

simulated patterns closely matched experimental observations under both unpolarized and polarized imaging conditions for both symmetric and asymmetric field arrangements (**Fig. 3f, 3g** and **Supplementary Fig. 6**). Hidden patterns, invisible under unpolarized imaging (Fig. 3f,g,i), emerged upon introducing an output polarizer (Fig. 3f,g,ii) and became increasingly complex when both input and output polarizers were employed (Fig. 3f,g,iii). Independent cross-validation further confirmed the fidelity and reproducibility of the simulated patterns (**Supplementary Fig. 7**). These results establish a reliable, deterministic mapping between magnet array configurations and plasmonic responses, demonstrating that complex three-dimensional magnetic fields can be encoded into predictable polarization-dependent color patterns, suitable for high-capacity encoding of physical information.

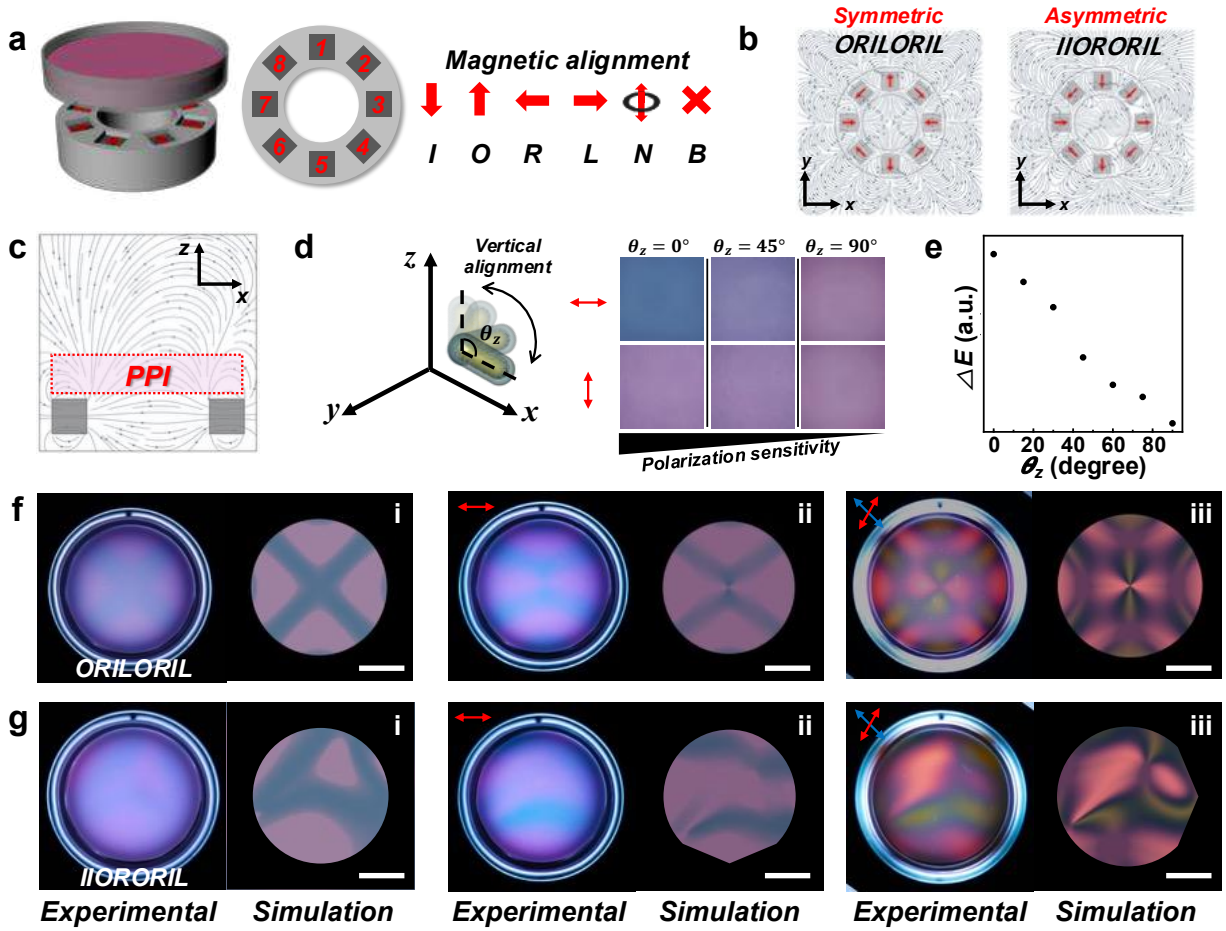


Fig. 3 | Experimental and simulated plasmonic color patterns generated by complex three-dimensional magnetic fields. a Schematic illustration of the customized circular holder containing eight cubic permanent magnets arranged at fixed angular intervals for generating programmable magnetic fields. **b** Representative periodic (*ORILORIL*) and aperiodic (*IIORORIL*) magnet arrangements generating symmetric and asymmetric three-dimensional magnetic field distributions, respectively. The magnetic field distributions were calculated using an analytical magnetostatic model[40]. **c** Cross-sectional magnetic field distribution on the x-z plane under the magnet setting of *IIORORIL*. The position of PPI relative to the magnet (grey block) is marked with red dotted lines. **d** Analyzer-angle dependence of plasmonic color as a function of the out-of-plane tilt angle (θ_z) under a single-polarizer configuration. **e** Color difference (ΔE) between vertical and horizontal analyzer polarization states as a function of θ_z. **f-g** Experimental plasmonic color patterns (left) and corresponding simulations (right) for a symmetric (f) and an asymmetric (g) magnetic field configurations under unpolarized (i), single polarizer (ii), and dual polarizer (iii) imaging conditions. Scale bar: (f) and (g) 1 cm.

Pixelated spatial encoding of plasmonic tags for enhanced encryption capacity

Pixelated spatial encoding transforms plasmonic color patterns into digitally encoded information while generating a vast encryption space. A hexagonal array of 60 microwells was fabricated, with each pixel assigned a unique cube-coordinate address to enable programmable placement of PPI at predefined spatial positions (**Fig. 4a**). As a representative example, a plasmonic tag generated using the *IIORORIL* magnetic configuration appeared optically featureless under unpolarized illumination, effectively concealing the encoded information (**Fig. 4b**). Introducing an output polarizer revealed a spatially multiplexed color pattern reflecting the underlying magnetic alignment (**Fig. 4c**). Employing both input and output polarizers further expanded the chromatic space, producing a richer and more discriminating optical readout (**Fig. 4d**). Thus, pixelation converts plasmonic color into addressable optical information, creating an encryption scheme in which polarization-resolved optical signatures and spatial addresses are jointly encoded. Varying the relative orientation of the input and output polarizers under the

dual-polarizer configuration further diversified the plasmonic color response, thereby increasing the encoding capacity (**Supplementary Fig. 8**).

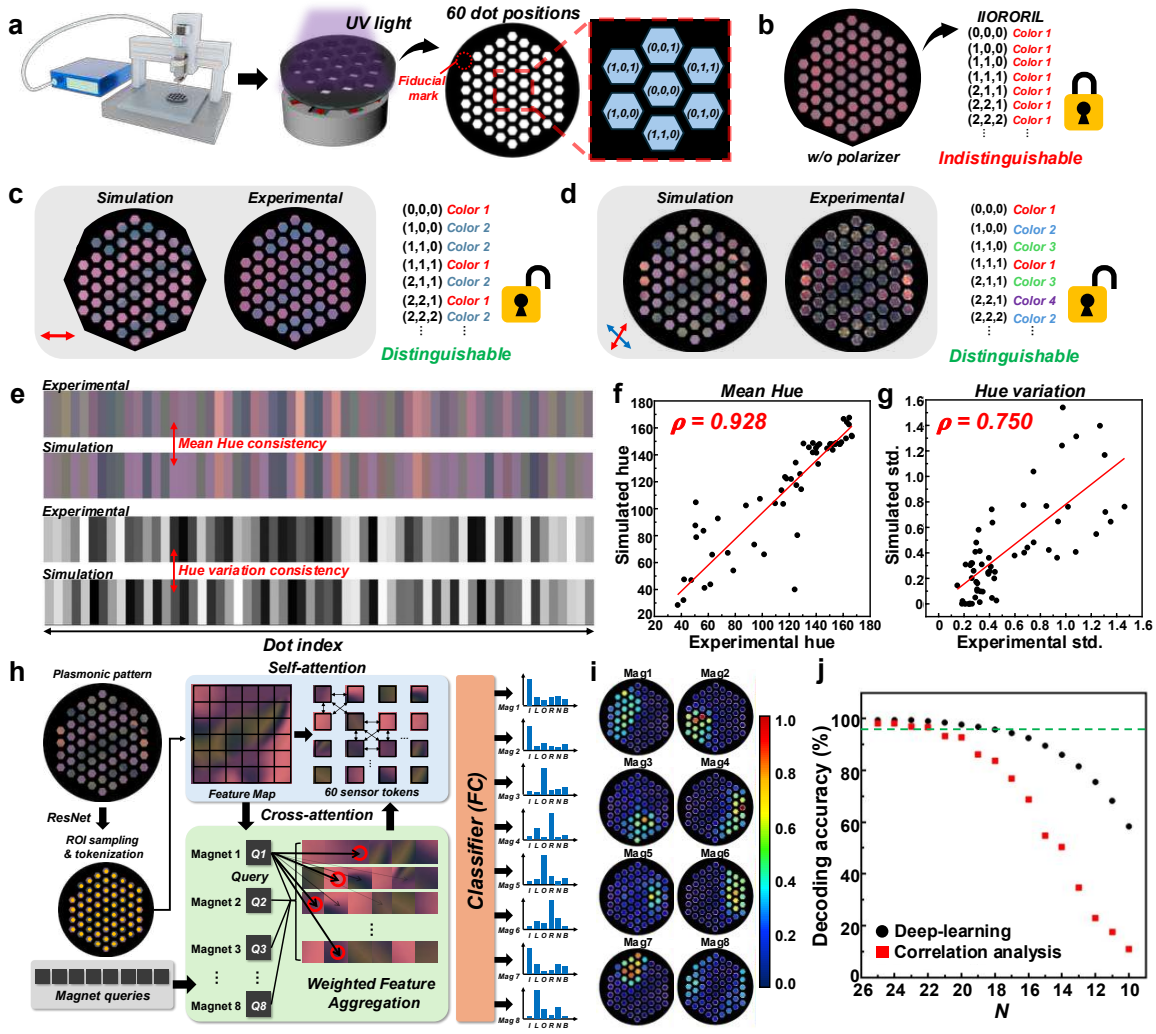


Fig. 4 | Encoding and decoding of pixelated plasmonic color via statistical analysis and deep learning. a Schematic for fabrication of pixelated plasmonic tag using a hexagonal microwell array and automated PPI dispensing. **b** Plasmonic tag fabricated under the *IIORORIL* magnetic configuration, appearing optically indistinguishable without polarizer. **c-d** Plasmonic color patterns revealed under (c) single- and (d) dual-polarizer configurations. **e** Comparison of experimentally measured and simulated mean hue values and hue variations extracted from each pixel in the plasmonic tag. The grayscale map represents the magnitude of normalized intra-pixel hue variation, where darker intensity indicates larger variation. **f-g** Spearman correlations between experimental and simulated plasmonic patterns for (f) mean hue values and (g) intra-pixel hue variations. **h** Schematic architecture of the supervised deep-learning decoder employing cross-attention to infer magnetic configurations ($\boldsymbol{M_i}$) from 60-pixel tokens. **i** Visualization of cross-attention weights, highlighting spatially selective pixel contributions during

magnetic configuration inference. **j** Decoding accuracy as a function of the number of observed pixels (N) for statistical correlation analysis and deep learning-based decoding.

Quantitative validation of plasmonic tags and deep-learning based decoding framework

To quantitatively validate the simulation framework, experimental and simulated tags were compared using mean hue and intra-pixel hue variation (**Fig. 4e**). Intra-pixel hue variation was included to account for local color heterogeneity arising from variations in MP orientation (**Supplementary Fig. 9**). Both descriptors showed strong correlations between experiment and simulation (ρ = 0.928 and 0.750, respectively; **Fig. 4f** and **4g**) and their combination uniquely identified the genuine tag among 120,000 simulated decoys (**Supplementary Note 4** and **Supplementary Fig. 10** and **11**).

We trained a supervised Transformer-based decoder incorporating cross-attention to infer the magnetic configuration (M_i), directly from pixelated plasmonic patterns (**Fig. 4h** and **Supplementary Note 5**). Despite being trained exclusively on simulated data, the decoder accurately inferred M_i from experimentally generated plasmonic tags. Visualization of the cross-attention weights revealed that the decoder selectively attended to a subset of pixels when inferring M_i (**Fig. 4i**), indicating that the model learned which regions of the plasmonic tag were most informative for decoding.

We quantified the minimum amount of pixel information required for reliable decoding by defining the decoding threshold (N_{th}) as the minimum number of observed pixels required to exceed 95% identification accuracy (**Fig. 4j**). Partial-observation datasets were generated by repeatedly and randomly subsampling N pixels from the 60-pixel array using 120,000 simulated plasmonic tags (**Supplementary Note 6**). Remarkably, the decoder correctly inferred M_i using as few as 17 of the 60 available pixels ($N_{\mathrm{th}}^{\mathrm{DL}} \approx 17$), whereas statistical correlation analysis required approximately 22 pixels ($N_{\mathrm{th}}^{\mathrm{Stat}} \approx 22$) to distinguish the genuine tag from

decoys. These results demonstrate that magnetic configurations can be reliably decoded from incomplete plasmonic tags, highlighting the high information density of the encoding strategy described here.

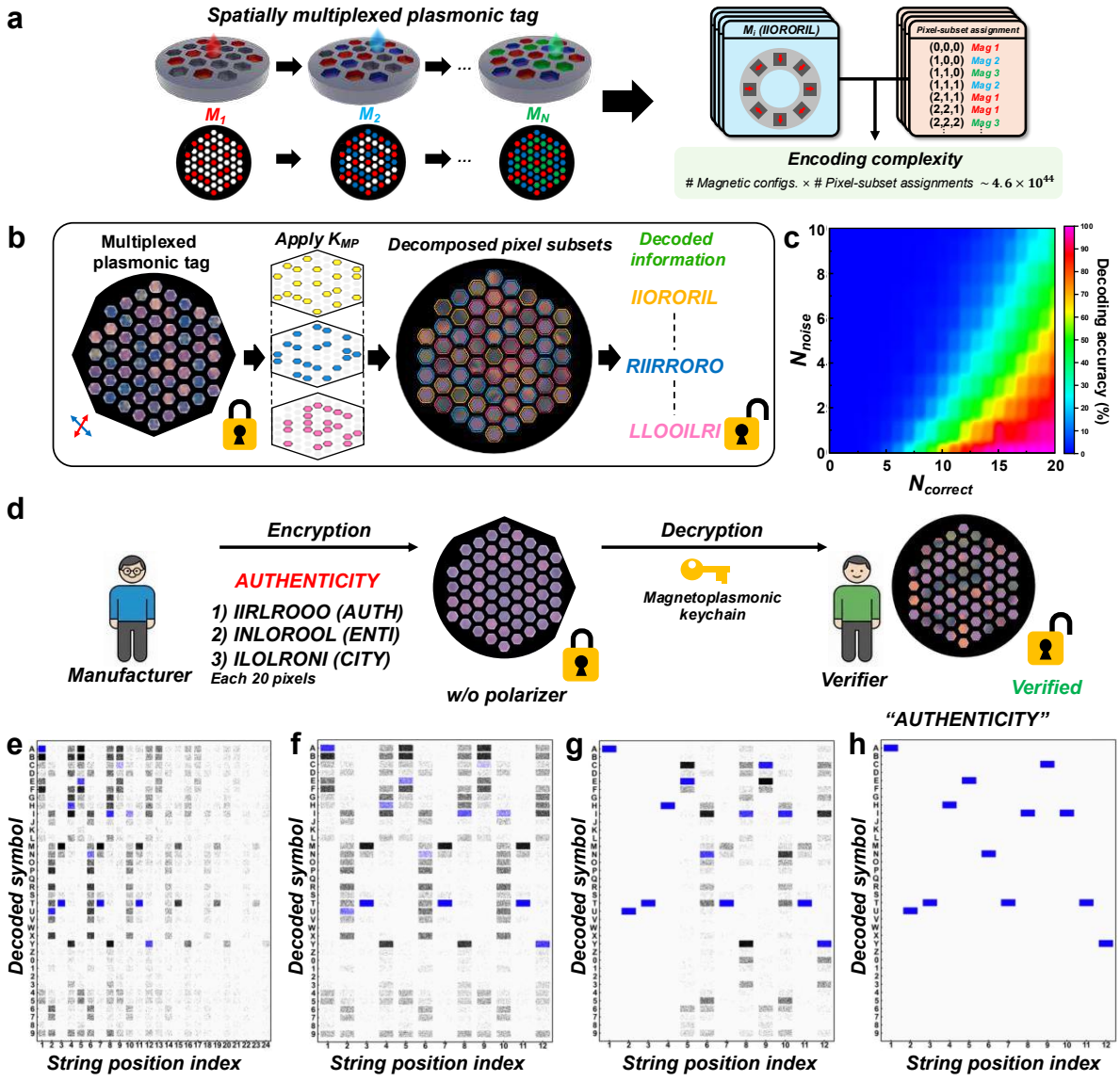


Fig. 5 | Magnetoplasmonic keychain-enabled multiplexed plasmonic encryption and authentication. a Schematic illustration of multiplexed plasmonic encoding by assigning three magnetic field configurations to three indexed subsets of pixels within a 60-pixel array, thereby defining the magnetoplasmonic keychain ($\boldsymbol{K_{MP}}$). **b** $\boldsymbol{K_{MP}}$-guided decomposition of a multiplexed plasmonic pattern into pixel subsets ($\boldsymbol{\Phi_i}$) corresponding to individual magnetic field configurations. **c** Heatmap of decoding accuracy as a function of pixel composition. $N_{correct}$ and N_{noise} denote the numbers of pixels o assigned to the target subset $\boldsymbol{\Phi_i}$ and the remaining subsets, $\boldsymbol{\Phi_j}(\boldsymbol{j \neq i})$, respectively. **d** Schematic of encryption and authentication. Plasmonic tags are generated during manufacturing, whereas decoding

during authentication requires both polarization-resolved optical readout and the complete $\boldsymbol{K_{MP}}$. **e-h** Statistical distribution of decoded characters obtained from 10,000 decoding trials of a 12-character symbolic pattern ("AUTHENTICITY") under different levels of access to the $\boldsymbol{K_{MP}}$. In each trial, pixel subsets ($\boldsymbol{\Phi_i}$) were randomly selected to infer the corresponding magnetic configurations. Each column represents a character position, and each row an alphanumeric character. Character frequencies at each position are indicated by color intensity, with the ground-truth character highlighted in blue. **(e)** Neither the $\boldsymbol{N_f}$ nor the $\boldsymbol{\Phi_i}$ is available. Pixel subsets of varying sizes are randomly generated. **(f)** $\boldsymbol{N_f}$ is available whereas $\boldsymbol{\Phi_i}$ remains unavailable. **(g)** $\boldsymbol{N_f}$ and a single $\boldsymbol{\Phi_i}$ are available. **(h)** The complete $\boldsymbol{K_{MP}}$, including both the $\boldsymbol{N_f}$ and all $\boldsymbol{\Phi_i}$, is available.

Ill-posed inverse mapping enables key-dependent multiplexed encryption

Magnetic configurations (M_i) can be spatially multiplexed within a single plasmonic tag by assigning each configuration to a distinct pixel subset, Φ_i, thereby creating a large encoding space (**Fig. 5a**). We define the corresponding magnetoplasmonic key as $K_{MP} = \left\{N_f, \{\Phi_i\}_{i=1}^{N_f}\right\}$ where N_f denotes the number of multiplexed magnetic configurations and Φ_i specifies the indexed pixel subset assigned to M_i. In essence, K_{MP} specifies how multiple magnetic configurations are spatially assigned within the multiplexed plasmonic tag. Because the deep-learning decoder requires only $N_{\text{th}}^{DL} \approx 17$ pixels for reliable decoding, a 60-pixel plasmonic tag can accommodate up to three independently decodable magnetic configurations while maintaining reliable inference, yielding an encoding space on the order of 10^{44}.

Importantly, the security of this scheme does not primarily originate from its large combinatorial encoding space. Rather, it arises because reconstructing the encoded magnetic configurations without K_{MP} is fundamentally an ill-posed inverse problem. Whereas the forward mapping from M_i to plasmonic color patterns is deterministic and reproducible, the inverse mapping is not uniquely defined in the absence of K_{MP}. Without the pixel-subset assignments specified by K_{MP}, a multiplexed plasmonic tag cannot be uniquely decomposed into its constituent magnetic configurations, precluding recovery of the encoded information.

Consequently, even a trained decoder cannot uniquely infer the encoded magnetic configurations without access to K_{MP}.

The role of K_{MP} is illustrated in **Fig. 5b**, where the multiplexed plasmonic tag is first decomposed into its constituent pixel subsets before independently decoding the corresponding magnetic configurations. To quantify the dependence on K_{MP}, decoding performance was evaluated by systematically perturbing the pixel assignments defined by the key (**Fig. 5c**). Decoding accuracy deteriorated rapidly as incorrectly assigned pixels were introduced, demonstrating that plasmonic color patterns alone do not uniquely determine the encoded magnetic configurations.

To extend this framework beyond pattern authentication, magnetic configurations were translated into symbolic information (**Fig. 5d**). Individual magnetic states were mapped to alphanumeric characters using a predefined encoding rule, in which two adjacent magnetic states were converted into a single character through a modulo-6 operation, allowing each M_i to encode a four-character symbolic string (**Supplementary Table 1**). Consequently, messages such as *AUTHENTICITY* can be physically embedded into a multiplexed plasmonic tag through magnetic patterning.

Fig. 5e-h evaluate symbolic decoding under progressively increasing access to K_{MP}, assuming that the trained decoder is available (**Supplementary Movie 1**). When neither N_f nor Φ_i was provided, recovered characters were statistically indistinguishable from random guessing (**Fig. 5e**). Knowledge of N_f alone resulted in similarly poor decoding performance (**Fig. 5f**), whereas disclosure of a single Φ_i yielded only marginal improvement (**Fig. 5g**). Reliable symbolic decoding was achieved only when the complete magnetoplasmonic key, K_{MP}, including both N_f and all Φ_i was available (**Fig. 5h**). These results demonstrate that symbolic information encoded in multiplexed plasmonic tags cannot be uniquely recovered without K_{MP},

regardless of the decoding algorithm employed, because the underlying inverse mapping is fundamentally ill-posed.

Conclusion

This study establishes a magnetoplasmonic platform that deterministically converts diverse three-dimensional magnetic field configurations into polarization-resolved optical states through magnetic alignment of plasmonic nanorods. Integrating magnetic field programming with spatially addressable photopatterning expands the accessible information space, enabling complex field configurations to be physically encoded into matter as decodable optical patterns. These physically programmed patterns constitute the basis of the proposed K_{MP}. The defining feature of the K_{MP} is its asymmetric accessibility. Thus, security arises from the inaccessibility of the key rather than computational complexity, establishing a physically enforced encryption process.

The K_{MP} exhibits favorable scaling characteristics. Because the K_{MP} is defined jointly by independent magnetic configurations and their spatial assignments, the accessible key space scales combinatorially with the number of addressable pixels. Combined with rapid magnetic alignment and photopolymerization, this architecture provides a scalable route toward physically encoded optical tags. More broadly, this study demonstrates that cryptographic functionality can be embedded directly into material systems, where security is governed by physical processes rather than algorithmic secrecy. By coupling deterministic encoding with key-dependent, non-unique inverse recovery, the K_{MP} provides a versatile foundation for next-generation security technologies including anti-counterfeiting, authentication, and information storage.

Acknowledgements

The authors acknowledge the use of AI-assisted language editing to refine the English expression of the manuscript based on author-provided content, as well as professional English editing services provided by EssayReview. All scientific content, interpretation, and conclusions were developed and verified by the authors, who take full responsibility for the work.

Funding

S.J.P. and T.S.S. are supported by the Ministry of Education of the Republic of Korea and the National Research Foundation of Korea (RS-2024-00397807). T.S.S. is supported by the Ministry of Education of the Republic of Korea and the National Research Foundation of Korea (RS-2026-25471872). S.J.P. is supported by the Ministry of Education of the Republic of Korea and the National Research Foundation of Korea (RS-2023-00274736, RS-2025-16063688).

Author contributions

J.H.P. and H.K. contributed equally to this work. J.H.P, S.J.P., and T.S.S. conceived the study. J.H.P. and T.S.S. developed the methodology. J.H.P., H.K., S.L., and Y.E.C. performed the investigations. J.H.P., H.K., and T.S.S. carried out the visualization. S.J.P. and T.S.S. acquired funding, administered the project, and supervised the research. The manuscript was originally drafted by J.H.P., T.S.S., and S.J.P.. J.H.P., H.K., H.H., S.J.P., and T.S.S. reviewed and edited the manuscript.

Competing interests

Authors declare that they have no competing interests.

Data and materials availability

All data supporting the findings of this study are available in the main text or the supplementary materials.

Code availability

The code used for magnetic-field simulations, plasmonic color-pattern and tag generation, and deep-learning-based decoding is available at https://github.com/JinhyeokPark-ajou/Magnetoplasmonic-keychain.

Supplementary Information

The Supplementary Information file includes Methods, Supplementary Notes 1-6, Supplementary Figs. 1-11, Supplementary Table 1 and Supplementary Movie 1.

References

1. Gandla, S. *et al.* Random laser ablated tags for anticounterfeiting purposes and towards physically unclonable functions. *Nat. Commun.* **15**, 7592 (2024).

2. Prime, E. L. & Solomon, D. H. Australia's Plastic Banknotes: Fighting Counterfeit Currency. *Angew. Chem. Int. Ed.* **49**, 3726–3736 (2010).

3. Yoon, B. *et al.* Recent functional material based approaches to prevent and detect counterfeiting. *Journal of Materials Chemistry C* **1**, 2388–2403 (2013).

4. Kim, J. J., Bong, K. W., Reátegui, E., Irimia, D. & Doyle, P. S. Porous microwells for geometry-selective, large-scale microparticle arrays. *Nat. Mater.* **16**, 139–146 (2017).

5. Fang, X., Ren, H. & Gu, M. Orbital angular momentum holography for high-security encryption. *Nat. Photonics* **14**, 102–108 (2020).

6. Diffie, W. & Hellman, M. New directions in cryptography. *IEEE Trans. Inf. Theory* **22**, 644–654 (1976).

7. Shannon, C. E. A mathematical theory of communication. *The Bell System Technical Journal* **27**, 379–423 (1948).

8. Rührmair, U. *et al.* Modeling attacks on physical unclonable functions. in *Proceedings of the 17th ACM Conference on Computer and Communications Security* 237–249 (Association for Computing Machinery, New York, NY, USA). (2010)

9. Yun, H. S. *et al.* Reconfigurable liquid crystal-based physical unclonable function integrating optical and electrical responses. *Adv. Mater.* **37**, 2504288 (2025).

10. Xiong, B. *et al.* Breaking the limitation of polarization multiplexing in optical metasurfaces with engineered noise. *Science* **379**, 294–299 (2023).

11. Zheng, H. *et al.* Uncovering the circular polarization potential of chiral photonic cellulose films for photonic applications. *Adv. Mater.* **30**, 1705948 (2018).

12. Kim, I. *et al.* Pixelated bifunctional metasurface-driven dynamic vectorial holographic color prints for photonic security platform. *Nat. Commun.* **12**, 3614 (2021).

13. Wan, W., Gao, J. & Yang, X. Full-color plasmonic metasurface holograms. *ACS Nano* **10**, 10671–10680 (2016).

14. Li, X. *et al.* Multicolor 3D meta-holography by broadband plasmonic modulation. *Sci. Adv.* **2**, e1601102 (2016).

15. Ren, H. *et al.* Complex-amplitude metasurface-based orbital angular momentum holography in momentum space. *Nat. Nanotech.* **15**, 948–955 (2020).

16. Gao, X. *et al.* Discontinuous orbital angular momentum metasurface holography. *Nat. Commun.* **16**, 10688 (2025).

17. Luo, X. *et al.* Integrated metasurfaces with microprints and helicity-multiplexed holograms for real-time optical encryption. *Adv. Opt. Mater.* **8**, 1902020 (2020).

18. Yu, Z. *et al.* High-security learning-based optical encryption assisted by disordered metasurface. *Nat. Commun.* **15**, 2607 (2024).

19. Ye, W. *et al.* Spin and wavelength multiplexed nonlinear metasurface holography. *Nat. Commun.* **7**, 11930 (2016).

20. Yoo, B. *et al.* High-throughput multiplexed plasmonic color encryption of microgel architectures via programmable dithering-mask flow microlithography. *Adv. Mater.* **37**, 2405388 (2025).

21. Wang, X. *et al.* Anisotropically shaped magnetic/plasmonic nanocomposites for information encryption and magnetic-field-direction sensing. *Research* **2018**, 7527825 (2018).

22. Lu, W., Chow, T. H., Lai, S. N., Zheng, B. & Wang, J. Electrochemical switching of plasmonic colors based on polyaniline-coated plasmonic nanocrystals. *ACS Appl. Mater. Interfaces* **12**, 17733–17744 (2020).

23. Murphy, C. J. *et al.* Anisotropic metal nanoparticles: synthesis, assembly, and optical Applications. *J. Phys. Chem. B* **109**, 13857–13870 (2005).

24. Chen, Y., Yang, X. & Gao, J. 3D Janus plasmonic helical nanoapertures for polarization-encrypted data storage. *Light: Science & Applications* **8**, 45 (2019).

25. Cheng, F., Gao, J., Luk, T. S. & Yang, X. Structural color printing based on plasmonic metasurfaces of perfect light absorption. *Sci. Rep.* **5**, 11045 (2015).

26. Kumar, K. *et al.* Printing colour at the optical diffraction limit. *Nat. Nanotech.* **7**, 557–561 (2012).

27. Duan, X., Kamin, S. & Liu, N. Dynamic plasmonic colour display. *Nat. Commun.* **8**, 14606 (2017).

28. Wu, B. *et al.* Laser-induced plasmonic nanostructures for optical storage and encryption in disordered crystals. *Adv. Opt. Mater.* **14**, e03136 (2026).

29. Guan, Y. *et al.* Far-field femtosecond laser-driven λ/73 super-resolution fabrication of 2D van der Waals NbOI2 nanostructures in ambient air. *Nat. Commun.* **16**, 4149 (2025).

30. Choi, W. *et al.* Helical photonic metamaterials for encrypted chiral holograms. *Adv. Sci.* **12**, e07931 (2025).

31. Lee, Y. H. *et al.* Hierarchically manufactured chiral plasmonic nanostructures with gigantic chirality for polarized emission and information encryption. *Nat. Commun.* **14**, 7298 (2023).

32. Lv, J. *et al.* Spatiotemporally modulated full-polarized light emission for multiplexed optical encryption. *Nat. Commun.* **15**, 8257 (2024).

33. Wang, H.-C. & Martin, O. J. F. Polarization-controlled chromo-encryption. *Adv. Opt. Mater.* **11**, 2202165 (2023).

34. Kim, J. *et al.* Dual chromic–dichroic modulation in plasmonic metasurfaces for enantioselective electrochromism. *ACS Nano* **19**, 35992–36001 (2025).

35. Li, J. *et al.* Addressable metasurfaces for dynamic holography and optical information encryption. *Sci. Adv.* **4**, eaar6768 (2018).

36. Kang, H. *et al.* Dynamic birefringence and chirality of magnetically controllable assemblies of anisotropic plasmonic nanoparticles in dispersion. *Nat. Commun.* **16**, 7076 (2025).

37. Li, Z., Jin, J., Yang, F., Song, N. & Yin, Y. Coupling magnetic and plasmonic anisotropy in hybrid nanorods for mechanochromic responses. *Nat. Commun.* **11**, 2883 (2020).

38. Wu, C. *et al.* Magnetically tunable one-dimensional plasmonic photonic crystals. *Nano Lett.* **23**, 1981–1988 (2023).

39. Li, Z. *et al.* Creation and reconstruction of thermochromic Au nanorods with surface concavity. *J. Am. Chem. Soc.* **143**, 15791–15799 (2021).

40. Ortner, M. & Coliado Bandeira, L. G. Magpylib: A free Python package for magnetic field computation. *SoftwareX* **11**, 100466 (2020).

Supplementary Files

This is a list of supplementary files associated with this preprint. Click to download.

- SupplementaryMovie1.mp4
- NCommPlasmonicKeychainSIv2.docx